Cross sections of the ^{20}Ne(n, α)^{17}O reaction in the 8.9 – 11.5 MeV neutron energy region*

Wenkai Ren (任文凯)[1] Jie Liu (刘杰)[1] Zepeng Wu (邬泽鹏)[1,2] Haofan Bai (白浩帆)[1] Cong Xia (夏聪)[1]
Yu. M. Gledenov[3] E. Sansarbayar[3,4] G. Khuukhenkhuu[4] I. Chuprakov[3,5] Xichao Ruan (阮锡超)[6]
Hanxiong Huang (黄翰雄)[6] Jie Ren (任杰)[6] Xiaofei Wang (王晓飞)[6] Bin Shao (邵斌)[6] Li'ao Zhao (赵立奥)[6]
Wentian Cao (曹文田)[1] Shixiang Peng (彭士香)[1] Tieshuan Fan (樊铁栓)[1] Guohui Zhang (张国辉)[1†]

[1]State Key Laboratory of Nuclear Physics and Technology, Institute of Heavy Ion Physics, School of Physics, Peking University, Beijing 100871, China
[2]National Key Laboratory of Intense Pulsed Radiation Simulation and Effect, Northwest Institute of Nuclear Technology, Xi'an 710024, China
[3]Frank Laboratory of Neutron Physics, Joint Institute for Nuclear Research, Dubna 141980, Russia
[4]Nuclear Research Centre, National University of Mongolia, Ulaanbaatar, Mongolia
[5]The Institute of Nuclear Physics, Ministry of Energy of the Republic of Kazakhstan, Almaty 050032, Kazakhstan
[6]China Institute of Atomic Energy, Beijing 102413, China

Abstract: State-resolved cross sections for the ^{20}Ne(n, α_i)^{17}O (i=0,1,2,3) reactions were measured in the 8.9 – 11.5 MeV neutron energy region (11 energy points) at the HI-13 tandem accelerator of the China Institute of Atomic Energy (CIAE). The present measurements extend the data of the α_0, α_1, α_2, and α_3 channels from 9.6 MeV to 11.5 MeV, where previous measurements reported only the summed (α_0+ α_1) cross sections. A twin gridded ionization chamber (GIC) filled with a neon-based gas mixture was used as the charged-particle detection, with the neon gas serving as an active sample. Corrections for detector efficiency, background interference, and neutron-field non-uniformity were performed by combining experimental measurements and detailed Monte Carlo simulations. From 9.6 to 11.5 MeV, the measured ^{20}Ne(n, α_0)^{17}O and ^{20}Ne(n, α_1)^{17}O cross sections decrease as neutron energy increases, and are generally consistent with those in JENDL-5. The ^{20}Ne(n, α_2)^{17}O cross sections are generally above those in JENDL-5, whereas the ^{20}Ne(n, α_3)^{17}O cross sections are below those in JENDL-5. In detail, the measured excitation functions exhibit noticeable fluctuations that are not included in JENDL-5. The TALYS-2.2 calculations can describe the measured α_0, α_1 and α_2 cross sections reasonably, whereas the calculated α_3 cross sections are generally higher than the measured α_3 cross sections. The present data provide new state-resolved constraints for modeling the ^{20}Ne(n, α)^{17}O reaction and improving nuclear data evaluation.

Keywords: cross sections, ^{20}Ne(n, a)^{17}O, neutron nuclear data

DOI: **CSTR:** 32044.14.ChinesePhysicsC.CPC-2026-0670

CPC Accepted

I. INTRODUCTION

Neon is a chemically inert gas element. Natural neon consists predominantly of ^{20}Ne (90.48%), with smaller contributions from ^{21}Ne (0.27%) and ^{22}Ne (9.25%).

The ^{20}Ne(n, α)^{17}O reaction (Q = – 0.587 MeV) is of considerable interest for studies of neutron-induced reactions on light nuclei. Owing to its relatively simple nuclear structure and the presence of several reaction channels, this reaction provides a valuable testing ground for nuclear reaction mechanisms, including compound-nucleus, pre-equilibrium, and direct reaction mechanisms [1]. For light nuclei, the relatively low-level density and the importance of individual discrete levels make statistical-model calculations less strongly averaged than in heavier nuclei. For neutron-induced (n, α) reactions on light nuclei, the neutron and α-particle optical-model potentials determine the entrance-channel and exit-channel transmission coefficients, while the level-density model and width-fluctuation correction affect the statistical decay of the compound nucleus and the branching among the open channels. Therefore, reliable cross sections, especially for state-resolved α-emission channels, are essential for constraining the data in evaluated nuclear data libraries and improving the description of neutron-induced reactions in

Received 1 August 2026; Accepted 9 October 2026

* The present work was financially supported by the Key Laboratory of Nuclear Data foundation (JCKY2025201C153), and the National Natural Science Foundation of China (Grant No. 12475299)

† E-mail: guohuizhang@pku.edu.cn

©2026 Chinese Physical Society and the Institute of High Energy Physics of the Chinese Academy of Sciences and the Institute of Modern Physics of the Chinese Academy of Sciences and IOP Publishing Ltd. All rights, including for text and data mining, AI training, and similar technologies, are reserved.

the light-mass region. In addition, this reaction is the inverse of the astrophysical neutron source reaction ^{17}O(α, n)^{20}Ne, which impacts on the weak *s* process in massive stars [2–5]. The study of the ^{20}Ne(n, α)^{17}O reaction can provide complementary information on the compound nucleus ^{21}Ne and on the reaction mechanisms in both forward and inverse processes. Possible α-cluster configurations in ^{20}Ne and ^{21}Ne have been discussed in previous studies [6,7]. While the present measurement does not provide a direct test of these cluster configurations, the state-resolved ^{20}Ne(n, α_i)^{17}O cross sections offer useful experimental information on α-emission branching and reaction-channel competition in the ^{21}Ne compound system.

In the neutron-energy region below 12 MeV, the ^{20}Ne(n, α)^{17}O reaction can be described mainly by the formation and decay of the compound nucleus ^{21}Ne, with α-particle emission populating the ground and low-lying excited states of ^{17}O [8]. As shown in Fig. 1, the ^{20}Ne(n, α)^{17}O reaction can be divided into partial channels ^{20}Ne(n, α_i)^{17}O (i=0,1,2,3) according to the final states populated in the residual nucleus ^{17}O. Because these low-lying states are well separated in energy, the corresponding α events can be distinguished experimentally, allowing state-resolved cross sections to be extracted.

Previous measurements of the ^{20}Ne(n, α)^{17}O reaction are rather limited and cover only selected neutron energy regions. Owing to the difficulty of preparing solid neon targets, all existing measurements utilized neon gas as an active target within ionization chambers or in gridded ionization chambers. Johnson *et al.* [9] measured the ^{20}Ne(n, α)^{17}O reaction cross section below about 3.4 MeV. Bell *et al.* [10] extended the measurements to the 2.8–4.4 MeV region and obtained partial cross sections for the α_0 and α_1 channels. Shamu *et al.* [11] further measured the α_0, α_1, α_2 and α_3 partial cross sections between 6.2 and 9.6 MeV, while only the summed α_0+α_1 cross sections were reported in the higher neutron energy region from 9.6 to 10.7 MeV. Although these measurements provided valuable information on the excitation functions of the ^{20}Ne(n, α)^{17}O reaction, the detector efficiencies and background contributions were not fully evaluated in the earlier works, which may have introduced sizable systematic uncertainties. Measurements near 14 MeV were later reported including the works of Cevolani *et al.* [12], McDicken *et al.* [13], Kardonsky *et al.* [14], and Lin *et al.* [15]. A recent measurement was performed by Khryachkov *et al.* (2012) [16] in the neutron-energy range from 4 to 7 MeV using a gridded ionization chamber filled with a Kr + Ne + CO_2 gas mixture. The α_0, α_1, α_2 and α_3 channels were identified by using the anode pulse height versus the anode signal rise time two-dimensional spectra. The influence of the pulse-height-defect (PHD) effect was present and discussed. Nevertheless, the separation of neighboring α particle groups remains challenging because of the overlap of the event regions in the two-dimensional spectra.

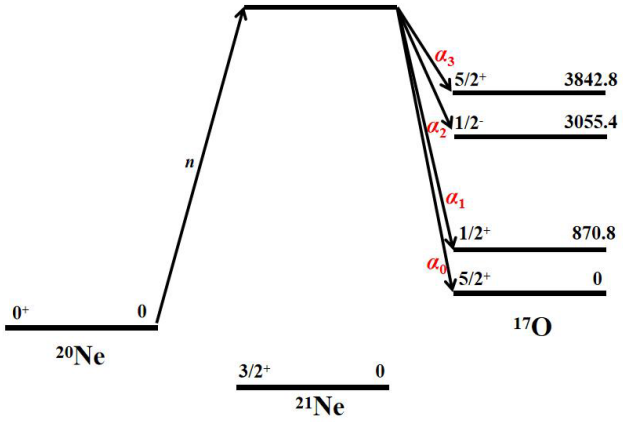


Fig. 1. (color online) Schematic level scheme of the ^{20}Ne(n, α)^{17}O reaction through the compound nucleus ^{21}Ne.

Due to the scarcity of experimental data, sizable discrepancies exist among different evaluated nuclear data libraries for the total ^{20}Ne(n, α)^{17}O reaction cross section, where the state-resolved channels are not distinguished [17]. This discrepancy is especially evident between ENDF/B-VIII.1 and JENDL-5 [17]. For the state-resolved channels, the available information in the evaluation libraries is even more limited. Among all of the evaluation libraries, only JENDL-5 [18] provides separate cross sections for the α_0, α_1, α_2 and α_3 channels. Therefore, new experimental cross sections for state-resolved reaction channels are needed to test and improve reaction-model calculations.

In recent years, our group has developed a measurement method based on the gas-sample and the gridded ionization chamber, neutron collimator, and detailed Monte Carlo simulations [19,20]. This method has been successfully applied in measurements of (n, α) reactions on light nuclei, including the ^{14}N(n, α)^{11}B [19] and ^{16}O(n, α)^{13}C [20]reactions. Our measurement method incorporates corrections for detector efficiency, background interference, the non-uniformity of neutron-field distribution, and low-energy neutron interference. In the present work, this method was further applied to the ^{20}Ne(n, α)^{17}O reaction. A twin gridded ionization chamber filled with a neon-based gas mixture was used, with natural neon component serving as the reaction sample. The cross sections for the ^{20}Ne(n, α_i)^{17}O (i=0,1,2,3) reaction channels were obtained in the neutron energy region of 8.9–11.5 MeV (11 energy points). In addition, because the α_0 and α_1 event regions are closely situated to each other in the measured spectra, the summed ^{20}Ne(n, α_0+α_1)^{17}O cross sections were also determined from the combined α_0+α_1 yields to provide a more reliable quantity for comparison with previous measurement and evaluation data. Compared with previous measurements, the present work

CPC Accepted

provides state-resolved experimental cross section data for the α_0, α_1, α_2 and α_3 channels from 9.6 to 11.5 MeV. Above 9.6 MeV, previous experimental data are only the summed α_0+α_1 cross sections reported by Shamu *et al.* [11]. The experimental setup of the present work is described in Sec. II, the data analysis is shown in Sec. III, the results are presented in Sec. IV, and the conclusions are drawn in the final section.

II. EXPERIMENTAL SETUP

The experiments were performed using the HI-13 tandem accelerator at the China Institute of Atomic Energy (CIAE). As shown in Fig. 2, the experimental setup includes four parts: the neutron source, the neutron collimator, the twin gridded ionization chamber (GIC) for charged particle detection, and the EJ-309 liquid scintillator for measurement of the neutron energy spectra.

Quasi mono-energetic neutrons were produced via the ^{2}H(d, n)^{3}He reaction. The neutron source consisted mainly of a deuterium gas target, separated from the accelerator vacuum tube by a 10.0-μm-thick molybdenum foil. The length of the gas cell was 3.0 cm and the diameter was 1.0 cm. The pressure of the deuterium gas in the cell was 2.0 atm. Measurements were performed in the neutron-energy range of 8.9–11.5 MeV, and the corresponding deuteron energy range was 6.4–8.9 MeV.

The neutron collimator was composed of pure copper material, which was placed between the neutron source and the GIC, as shown in Fig. 2. The detailed information of the design of the collimator and experimental validation can be found in our previous work [19]. The neutron flux distribution within the GIC was obtained through Geant4 simulation [21], as the R-Z plot shown in Fig. 3. The collimated region was approximately a cone. The horizontal (Z) axis corresponds to the direction of the incident neutron beam, while the vertical (R) axis represents the radial distance.

The region inside the red trapezoid in Fig. 3 of the 01 side corresponds to the main reaction volume (MRV). The real three-dimensional MRV in Fig. 2 is a circular truncated cone with the radii R_1 = 3.6 cm and R_2 = 4.0 cm, and it was used to calculate the average neutron fluence and the number of ^{20}Ne atoms. In the present work, only the 01 side of the GIC was used to measure the (n, α) events.

A twin GIC was used as the charged particle detector, whose measurement principle, structure and the electronics can be found in Ref. [22]. A high voltage of −2800 V was applied to the cathode, while + 1400 V was applied to the anodes, with the grid electrodes grounded. The cathode-grid and anode-grid distances were 6.1 and 1.4 cm, respectively. The working gas in the GIC was the 78.9%Kr + 20.0% Ne + 1.1% CH_4 mixture gas with the pressure of 4.5 atm at (23.7 ± 0.1) ^{o}C. The natural neon gas was the sample with the ^{20}Ne abundance of 90.48%. Description of the electronics can be found in Ref. [22]. It is worth emphasizing that the external trigger was generated by the coincidence of the anode and cathode signals of the GIC, which effectively suppressed electronic noise and background events. The typical counting rate was less than 500 events/s, and the dead-time and pulse pile-up effects were found to be negligible compared with the other uncertainty sources.

A sample changer with five sample positions was positioned at the common cathode of the GIC [19]. A back-to-back α-sources (^{234}U, 4.775 MeV; ^{239}Pu, 5.155 MeV; ^{238}Pu, 5.499 MeV; ^{244}Cm, 5.805 MeV) was set at sample position #1, and back-to-back Ta/$^{238}U_2O_3$#II was set at sample position #2, other three positions were all set with back-to-back Ta/Ta backings. The $^{238}U_3O_8$#I sample with 99.999% enrichment was glued on the center of the shield of the 01 side. The shield-anode distance was 1.0 cm. The diameter of the $^{238}U_3O_8$#I sample is 45.0 mm, and the

CPC Accepted

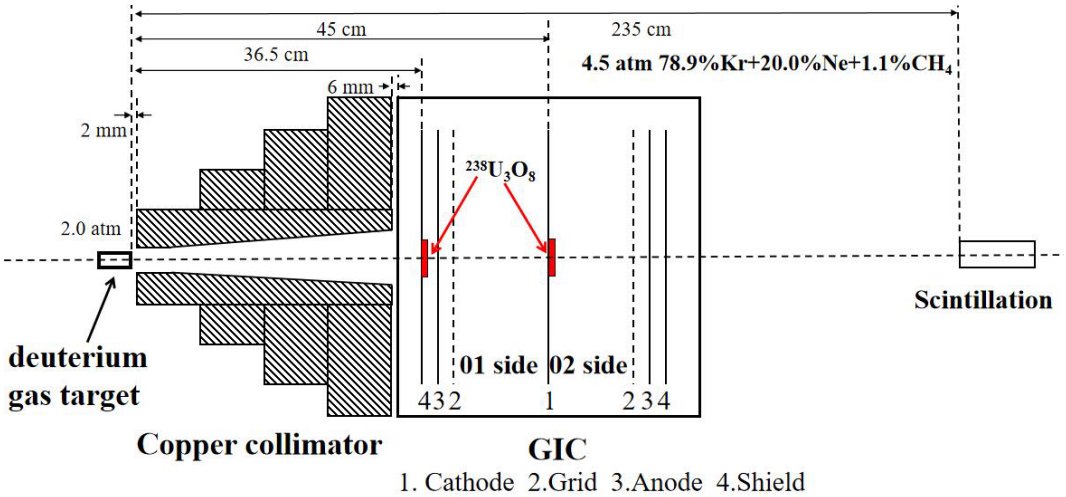


Fig. 2. (color online) Experimental Setup.

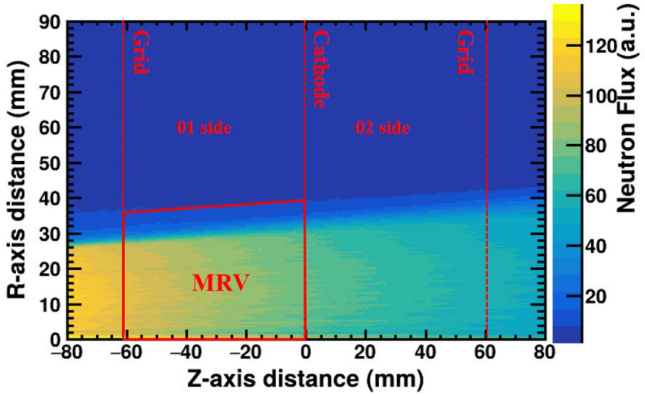


Fig. 3. (color online) The simulated neutron flux distribution inside the GIC.

nuclei number of ^{238}U ($N_{\rm U}$) is (2.081 ± 0.020) × 10^{19} [23]. In the present measurement, only the 01 side of the twin GIC was used for the ^{20}Ne(n, α)^{17}O event selection in the present work. The 02 side was used to place $^{238}U_3O_8$#II sample for fission event measurements, but the 02 side fission data were not included in the final analysis because of the low fission statistics and the relatively low fission-fragment detection efficiency caused by gas sample (n, α) events. This does not affect the present cross section determination, since the neutron fluence was obtained from the fission cathode measurement. Owing to the large number of ^{20}Ne atoms in the MRV ($N^{\rm MRV}_{\rm sample}$= 5.68×10^{21}), the statistical uncertainty of the selected (n, α) events was smaller than 1%. Therefore, using only the 01 side was sufficient to reduce the statistical uncertainty to an acceptable level in the present measurement.

An EJ-309 liquid scintillation detector was used to measure the neutron spectrum. The unfolding method was used to obtained the neutron spectrum [24,25]. In addition to the main-energy neutrons from the ^{2}H(d, n)^{3}He reaction, there are also low-energy neutrons, mainly from the ^{2}H(d, np)^{2}H reaction and scattering off the walls. The interference α events induced by the low-energy neutrons were corrected in Sec. III.

Only two sample positions were used in the present experiments: Firstly, the back-to-back compound α-sources mounted at sample position #1 was used for energy calibration of the detection system without the neutron beam. Secondly, back-to-back Ta/$^{238}U_2O_3$#II samples mounted at sample position #2 were used for the measurements of the events of the ^{20}Ne(n, α)^{17}O reaction from gas samples with the neutron beam on. The total neutron beam duration was ~ 18 h.

III. DATA ANALYSIS

The cross section (σ_α) of the ^{20}Ne(n, α)^{17}O reaction can be calculated from

$$\sigma_\alpha = \frac{N_{\rm event}}{\Phi_{\rm MRV}\cdot N_{\rm sample}}, \quad (1)$$

where $N_{\rm event}$ is the number of the (n, α) events, $N_{\rm sample}$ is the effective number of the ^{20}Ne nuclei, and $\Phi_{\rm MRV}$ is the average neutron fluence through the main reaction volume (MRV). Unlike experiments employing foil solid samples, the neon gas sample occupies an extended three-dimensional volume inside the GIC. As a result, the neutron fluence, reaction yield, and event-detection efficiency depend on the reaction position. To obtain accurate cross sections, correction factors associated with detector efficiency, background interference and the non-uniformity of neutron-field distribution in the GIC detector were evaluated using detailed Monte Carlo simulations and incorporated into the data analysis procedure. This treatment is more detailed in the present work than in previous measurements, together with the improved identification of the α_i event groups using the corrected anode-energy versus distance two-dimensional spectra (see Sec. III.A). This enables a more reliable determination of the state-resolved ^{20}Ne(n, α_i)^{17}O (i=0,1,2,3) cross sections.

A. Determination of the number of the α events

The measured anode energy versus anode signal rise time two-dimensional spectrum at $E_{\rm n}$ = 10.49 MeV is shown in Fig. 4(a). The rise time of the anode signal is proportional to the projection length of the charged-particle track along the electric-field direction [19]. As shown in Fig. 4(a), the α particle events can be clearly separated from proton events due to much shorter ranges of α particle in the working gas. In addition, the α_0, α_1, α_2 and α_3 event groups from the ^{20}Ne(n, α)^{17}O reaction corresponding to different energy states of ^{17}O can be identified. One can see from Fig. 4(a), each (n, α_i) (i=0,1,2,3) event group exhibits a characteristic V-shaped structure in the anode energy versus anode signal rise time two-dimensional spectrum [16,26]. This behavior originates from the pulse-height-defect (PHD) effect [26,27] in the gas ionization chamber. In our previous work, the impact of the PHD effect on measurements was analyzed, as detailed in [26]. As a result, the event groups corresponding to different (n, α_i) (i=0,1,2,3) channels partially overlap with each other, as shown in Fig. 4(a).

To better distinguish different (n, α_i) event groups, a linear coordinate transformation was applied to the anode energy versus anode signal rise time two-dimensional spectrum. The corrected anode energy was defined as

$$E_{\rm corr} = E_{\rm anode} - b(T_{\rm rise} - T_0), \quad (2)$$

where $E_{\rm anode}$ is the amplitude of the anode signal of the GIC, $T_{\rm rise}$ is the rise time of the anode signal, T_0 is the

CPC Accepted

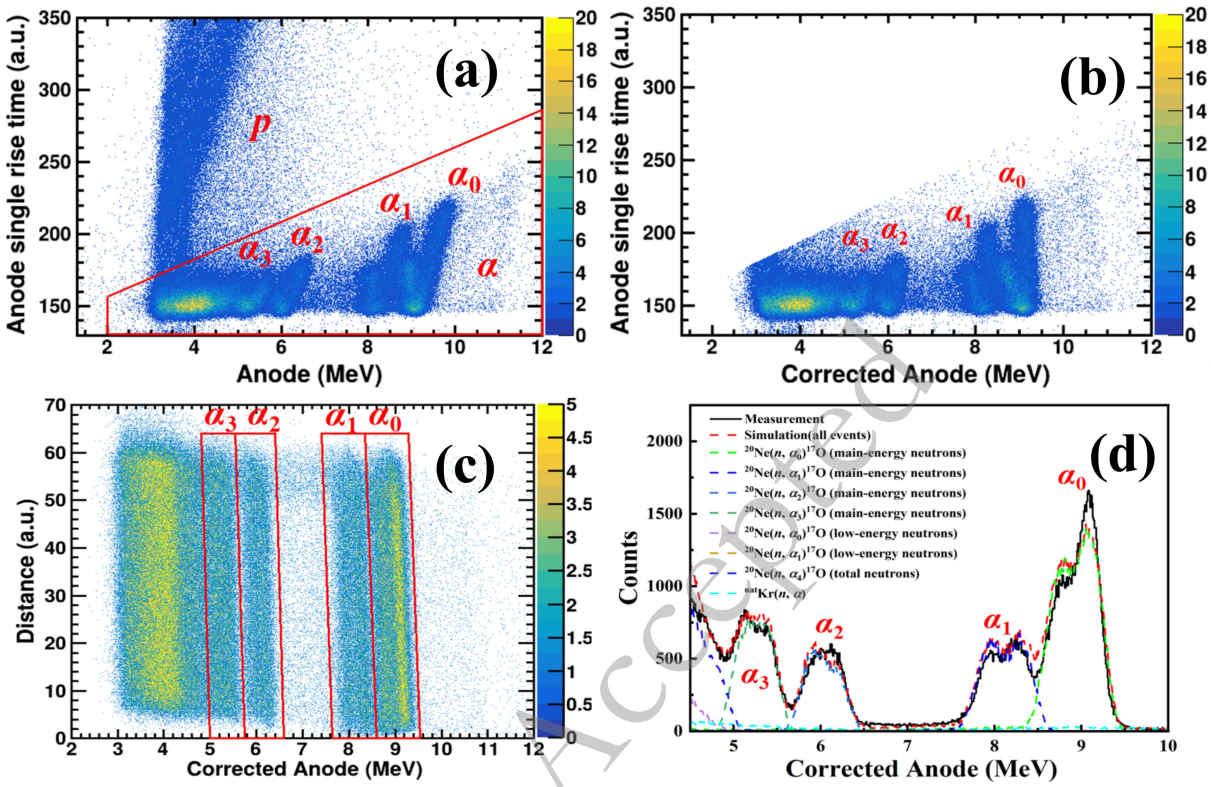


Fig. 4. (color online) The measured anode energy versus anode signal rise time two-dimensional spectrum (a), and corrected anode energy versus anode single rise time two-dimensional spectrum after the linear transformation (b), and corrected anode energy versus distance two-dimensional spectrum (c), and measured and simulated corrected anode energy spectra (d) at E_n = 10.49 ± 0.08 MeV.

minimum rise time of the anode signal, and b is the slope parameter determined from the tilted structures of the α_i event bands in the anode signal rise time versus anode amplitude 2D spectrum. In the present analysis, T_0 = 145 a.u. and b = 0.0095 MeV/a.u. were used. The spectrum after transformation is shown in Fig. 4(b), where the separation between different (n, α_i) event groups is significantly improved. However, after the transformation, neighbor event groups still partially overlap in the anode-energy spectrum, therefore additional position information was used to improve the event identification. The time difference between the starting times of the anode signal and cathode signal is proportional to the distance from the grid of the GIC to the closest point on the track of the detected α particle (hereinafter referred to as the "distance" [19]). The corrected anode energy versus "distance" two-dimensional spectra were obtained, as shown in Fig. 4(c). The (n, α_0), (n, α_1), (n, α_2) and (n, α_3) events were then selected separately, as indicated by the red rectangles in Fig. 4(c).

Detailed Monte Carlo simulations were performed by considering the individual ^{20}Ne(n, α_i)^{17}O (i=0,1,2,3) channels induced by both the main-energy and low-energy neutron components, together with the background contribution mainly from ^{nat}Kr(n, α) reactions. The cross sections of ^{nat}Kr(n, α) reactions were taken from ENDF/B-VIII.1 [28], while the cross sections of the ^{20}Ne(n, α_i)^{17}O (i=0,1,2,3) reactions were taken from JENDL-5 [18]. The simulated events were processed using the same coordinate transformation and selection conditions as those applied to the experimental data, and the corrected anode-energy versus distance two-dimensional spectra were generated. The event-selection regions shown in Fig. 4(c) were applied consistently to both the measured and simulated spectra to determine the detection efficiency and the correction factor for background interference. Figure 4(d) shows a representative comparison between the measured and simulated corrected anode energy spectra, demonstrating the reliability of the simulation-based corrections.

Based on our established gas-sample measurement method developed in Refs. [19,20], four correction factors were introduced to obtain the number of ^{20}Ne(n, α_i)^{17}O events. The number of the ^{20}Ne(n, α_i)^{17}O events was determined from [19,20]

$$N_{\text{event}} = \frac{N_\alpha \cdot k \cdot (1-\eta_\alpha^{\text{low}})}{\varepsilon_\alpha^{\text{amp}} \cdot \varepsilon_\alpha^{\text{dis}}}, \tag{3}$$

where N_α is the count of α events within the selected event region, as shown in Fig. 4(c). In addition to N_α, four correction factors were introduced. $\varepsilon_\alpha^{\text{amp}}$ is the anode

CPC Accepted

detection efficiency introduced to correct for event losses caused by the wall effect, which reduces the anode pulse amplitudes of some events and moves them outside the selected anode-energy region [19]. To better evaluate this efficiency and to improve the separation of the (n, α_0), (n, α_1), (n, α_2) and (n, α_3) events, the anode-energy selection was performed using the corrected anode-energy versus distance two-dimensional spectra shown in Fig. 4(c). The method of $\varepsilon_\alpha^{\rm amp}$ determination in the present work differs from our previous gas-sample measurements in Refs. [19,20], where the event selection was mainly based on the experimental anode-amplitude spectra. In addition, events occurring close to the grid may produce cathode signals with amplitudes below the lower threshold and therefore may escape identification, leading to a loss of events occurring near the grid region. This loss was corrected by introducing the detection efficiency for distance ($\varepsilon_\alpha^{\rm dis}$) [19]. k is the correction factor for background interference, and $\eta_\alpha^{\rm low}$ means the proportion of α events induced by low-energy neutrons within the threshold [19].

The selected event region of the individual ^{20}Ne(n, α_i)^{17}O (i=0,1,2,3) channels are indicated by the red rectangles in Fig. 4(c). The anode detection efficiency ($\varepsilon_\alpha^{\rm amp}$) was determined from the ratio of simulated events inside the selected region in the corrected anode energy versus distance two-dimensional spectra (Fig. 4(c)) to the total number of the simulated (n, α) events. The correction factor of background interference (k) was determined as the ratio of the number of the simulated (n, α_i) events to the total number of events inside the selected region, including (n, α_i) events to be measured, other (n, α_i) events and background events, in the corrected anode energy versus distance two-dimensional spectra. In addition, because low-energy neutrons in neutron energy spectrum also induced (n, α) events, the correction factor $\eta_\alpha^{\rm low}$ accounts for events induced by low-energy neutrons were considered. The detailed method used to determine the low-energy neutron correction can be found in Ref. [22]. The simulated distance spectrum, obtained without the cathode-threshold loss, was normalized to the measured spectrum in the reliable distance region defined by the lower and upper thresholds, as shown in Fig. 5. The detection efficiency for distance ($\varepsilon_\alpha^{\rm dis}$) was obtained by comparing the total counts of measured and simulated distance spectra.

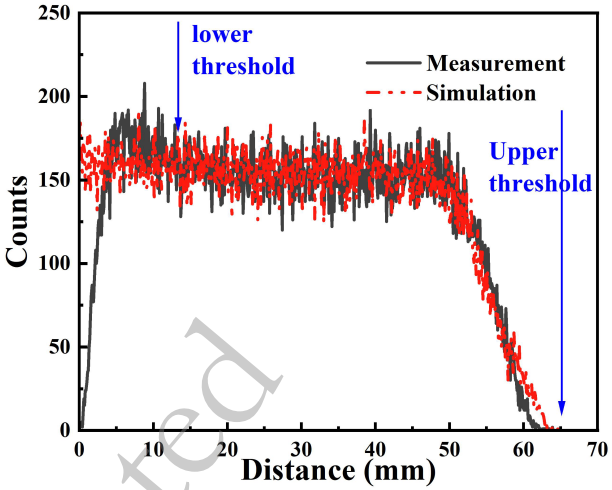


Fig. 5. (color online) The measured and simulated distance spectrum for ^{20}Ne(n, α_0)^{17}O reaction at $E_{\rm n}$ = 10.49 ± 0.08 MeV.

The simulations were performed for each neutron energy point to determine the values of $\varepsilon_\alpha^{\rm amp}$, $\varepsilon_\alpha^{\rm dis}$, k and $\eta_\alpha^{\rm low}$. The ranges of the values of these corrections for the individual ^{20}Ne(n, α_i)^{17}O (i=1,2,3,4) channels are shown in Table 1. The value of $\varepsilon_\alpha^{\rm amp}$ decreases as the neutron energy increases. The range of the charged particles becomes longer as the neutron energy increases, making the wall effect more pronounced and leading to a decrease in $\varepsilon_\alpha^{\rm amp}$. The value of $\varepsilon_\alpha^{\rm dis}$ generally increases as neutron energy increases. The correction factor for background interference (k) decreases as neutron energy increases, indicating an increasing background contribution, since (k) is defined as one minus the correction factor for background interference. The low-energy neutron contributions ($\eta_\alpha^{\rm low}$) are negligible for (n, α_0) and (n, α_1) channels, with values below 0.10%. However, it becomes more significant for (n, α_2) and (n, α_3) channels, reaching up to 13.96% and 33.31%, respectively, as shown in Table 1. This is mainly because the (n, α_0) and (n, α_1) events induced by low-energy neutrons can partially enter the selected (n, α_2) and (n, α_3) regions. For the (n, α_3) channel, the low-energy neutron contribution exceeds 10% only at

Table 1. Ranges of the values of the coefficient in Eq. (3)

Coefficient	Values (%)				
	^{20}Ne(n, α_0)^{17}O	^{20}Ne(n, α_1)^{17}O	^{20}Ne(n, α_2)^{17}O	^{20}Ne(n, α_3)^{17}O	^{20}Ne(n, α_0+α_1)^{17}O
$\varepsilon_\alpha^{\rm amp}$	88.35~92.98	90.24~94.50	92.54~96.81	94.48~97.84	91.83~95.83
$\varepsilon_\alpha^{\rm dis}$	95.51~98.66	94.90~99.28	90.28~95.01	88.67~94.72	95.89~99.28
k	92.39~99.59	81.49~99.65	86.45~93.63	82.48~89.85	87.83~99.22
$\eta_\alpha^{\rm low}$	< 0.10	< 0.10	0.60~13.96	1.06~33.31	< 0.10

CPC Accepted

the four neutron-energy points below 10 MeV, namely 8.94, 9.13, 9.44, and 9.69 MeV; above 10 MeV, this correction is relatively small. The uncertainty of this correction was evaluated by varying the low-energy neutron fraction by 10% and recalculating the corresponding correction factors.

Although the α_0 and α_1 events can be separated after the transformation, their event regions remain close, resulting in a relatively large uncertainty in the determination of the α_1 events. In addition, the previous measurements (Shamu *et al*. [11]) reported only the summed (α_0 + α_1) cross sections. Thus, the (α_0 + α_1) yield was also determined from the uncorrected anode-energy spectrum for comparison. The simulations for (α_0 + α_1) were performed for each neutron energy point to determine the values of $\varepsilon_\alpha^{\rm amp}$, $\varepsilon_\alpha^{\rm dis}$, k and $\eta_\alpha^{\rm low}$, which are also presented in Table 1.

B. Determination of the neutron fluence

The average neutron fluence through the MRV ($\phi_{\rm MRV}$) can be calculated by

$$\Phi_{\rm MRV} = \frac{\Phi {\rm u}}{G} = \frac{N_f \cdot (1-\eta_f^{\rm low})}{\sigma_f \cdot N_U \cdot \varepsilon_f \cdot G}, \tag{4}$$

where $\phi_{\rm U}$ is the average neutron fluence through the $^{238}U_3O_8$#1 sample at the shield of the GIC, and G is the ratio of the neutron fluence through the $^{238}U_3O_8$#1 sample to the average neutron fluence through the MRV, N_f is the measured fission counts, $\eta_f^{\rm low}$ is the corrected factor for low-energy neutron contribution, the σ_f is the cross sections of the ^{238}U(n, f) reaction, $N_{\rm U}$ is the ^{238}U atom number in the $^{238}U_3O_8$#1 sample, ε_f is the detection efficiency of fission fragments [22]. A typical fission spectrum of the fission fragments from the $^{238}U_3O_8$#1 is shown in Fig. 6. The fission counts (N_f) were obtained by integrating the spectrum within the selected lower and upper thresholds. The detection efficiency of fission fragments (ε_f) can be calculated from simulation [22]. It is calculated from the ratio of the fission events between the lower and upper thresholds in the simulated fission spectrum to the total number of the simulated fission events, as shown in Fig. 6. The obtained (ε_f) values range from 87.8% to 88.2%. In addition, the contribution of fission events induced by low-energy neutrons in the neutron energy spectrum was corrected by the factor ($\eta_f^{\rm low}$), which is determined using the method in Ref. [22]. The cross sections of the ^{238}U(n, f) reaction (σ_f) are taken from the IAEA-Std17 [29]. The ^{238}U atom number in the $^{238}U_3O_8$#1 sample ($N_{\rm U}$) is described in Sec. II.

Because the $^{238}U_3O_8$ sample and the neon gas sample occupy different positions in the GIC, the neutron fluence through the fission sample is not identical to the average neutron fluence in the main reaction volume

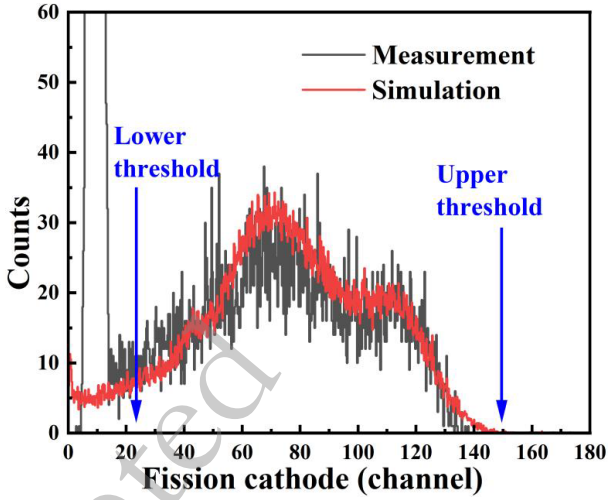


Fig. 6. (color online) Measured fission spectrum from the $^{238}U_3O_8$ sample at the shield at $E_{\rm n}$ =9.44 ± 0.08 MeV.

(MRV). Therefore, the simulated neutron-field distribution in the GIC, as shown in Fig. 3, was used to determine the fluence ratio (G). The obtained G values range from 1.81 to 1.82. A detailed description of the calculation method for (G) can be found in Ref. [19].

C. Determination of the ^{20}Ne atom number of the gas sample

The atom number of the ^{20}Ne sample ($N_{\rm sample}$) can be calculated by

$$N_{\rm sample} = N_{\rm sample}^{\rm MRV} \cdot W, \tag{5}$$

where $N_{\rm sample}^{\rm MRV}$ is the number of ^{20}Ne nuclei in the MRV, and W is the correction factor of the nuclei number for incomplete shielding of the collimator. The value of $N_{\rm sample}^{\rm MRV}$ was determined from the MRV volume, the gas pressure, the ratios of gas components, the gas temperature, and the isotopic abundance of ^{20}Ne using the ideal gas equation. Because the neutron collimator cannot provide complete shielding, a fraction of ^{20}Ne(n, α_i)^{17}O reactions may occur outside the MRV. Some of these events can still be recorded using the same selection rules as events generated inside the MRV and therefore will contribute to the measured yield. The correction factor (W) was calculated using Monte Carlo simulations and ranges from 1.267 to 1.297 in the present work. The value of W increases as neutron energy increases, indicating that the contribution of the events generated outside the MRV region becomes larger at higher neutron energies. A detailed description of the calculation method for W can be found in Ref. [19].

D. Uncertainty Analysis

The sources of the uncertainties and their magnitudes

CPC Accepted

are summarized in Table 2. The total uncertainty for each measured cross section was obtained by combining the individual uncertainty components listed in Table 2 in quadrature, i.e., using the root-sum-square method. The total uncertainties of the measured cross sections are 8.22% ~ 10.81% for the α_0 channel, 8.38% ~ 15.59% for the α_1 channel, 9.15% ~ 10.56% for the α_2 channel, 10.34% ~ 12.89% for the α_3 channel, and 7.58% ~ 10.98% for the $\alpha_0+\alpha_1$ channel. Because the gas atoms are distributed throughout the chamber and the neutron collimator cannot provide complete shielding, the uncertainty associated with the effective number of target nuclei ($N_{\rm sample}$) becomes a relatively important contribution in gas sample measurements. The correction factor (W), which accounts for the reactions generated outside the MRV due to incomplete collimator shielding, gives one of the largest systematic contributions, with uncertainties of about 5.3% ~ 6.1%. In addition, since dedicated background measurements were not performed and the background was subtracted using simulations instead, the background correction factor (k) also introduces a significant uncertainty, ranging from 0.78~12.04%. This contribution is particularly important for the α_1 channel, for which the maximum total uncertainty of 15.59% occurs at the highest measured neutron energy ($E_{\rm n}$ = 11.51 MeV) mainly because the neighboring α_0 events affected by the wall effect can partially enter the selected α_1 event region.

The uncertainty components listed in Table A1 are not all independent among different neutron energy points. For N_α, the uncertainty is dominated by the event-region selection, whereas the statistical uncertainty of the selected N_α events is smaller than 1% for all four reaction channels. This uncertainty was treated mainly as a point-to-point component, although it may also contain a small correlated contribution from the common event-selection procedure. In contrast, $N_{\rm u}$, $N_{\rm sample}^{\rm MRV}$ and the standard ^{238}U(n, f) cross section σ_f mainly contribute correlated normalization uncertainties. The correction factors $\varepsilon_\alpha^{\rm amp}$, $\varepsilon_\alpha^{\rm dis}$, k, ε_f, $\eta_\alpha^{\rm low}$, $\eta_f^{\rm low}$, G and W are energy dependent, but their uncertainties contain correlated components because they are derived from common experimental inputs, detector geometry, MRV definition, and simulation procedures. Therefore, the total uncertainties in Table A1 should not be regarded as fully point-to-point independent.

IV. RESULTS AND ANALYSIS

A. Measurement results

According to Eqs. (1), (3), (4) and (5), the cross sections of the ^{20}Ne(n, α_0)^{17}O, ^{20}Ne(n, α_1)^{17}O, ^{20}Ne(n, α_2)^{17}O, and ^{20}Ne(n, α_3)^{17}O reactions can be obtained.

The measured cross sections of the ^{20}Ne(n, α_i)^{17}O (i=0,1,2,3) reactions are shown in Fig. 7 and in Table A1 of Appendix A. The present α_0, α_1 and α_2 partial cross sections exhibit an overall decreasing trend as the neutron energy increases, although the excitation functions

Table 2. Sources of the uncertainties and their magnitudes.

Source	Magnitude (%)				
	^{20}Ne(n, α_0)^{17}O	^{20}Ne(n, α_1)^{17}O	^{20}Ne(n, α_2)^{17}O	^{20}Ne(n, α_3)^{17}O	^{20}Ne(n, $\alpha_0+\alpha_1$)^{17}O
N_α	0.63~1.21	1.38~3.55	1.27~2.55	2.48~3.67	0.34~0.70
$\varepsilon_\alpha^{\rm amp}$	3.51~5.82	2.75~4.88	1.60~3.00	1.08~2.58	0.21~0.41
$\varepsilon_\alpha^{\rm dis}$	1.33~2.46	1.51~3.58	2.51~4.92	2.73~5.67	0.85~2.29
k	2.37~5.10	2.80~12.04	4.22~6.51	5.02~7.01	0.78~6.92
$\eta_\alpha^{\rm low}$	< 0.1	< 0.1	0.12~2.77	0.21~6.66	< 0.1
N_f	0.97~1.57[a]	~	~	~	~
σ_f	1.40~1.50[a]	~	~	~	~
$N_{\rm u}$	1.00[a]	~	~	~	~
ε_f	2.38~2.41[a]	~	~	~	~
G	1.48~1.52[a]	~	~	~	~
$\eta_f^{\rm low}$	0.91~1.62[a]	~	~	~	~
$N_{\rm sample}^{\rm MRV}$	1.17[a]	~	~	~	~
W	5.34~6.05	5.44~5.99	5.28~5.58	5.34~5.70	5.34~6.03
σ_α	8.22~10.81	8.38~15.59	9.15~10.56	10.34~12.89	7.58~10.98

[a]For ^{20}Ne(n, α_i)^{17}O (i=0,1,2,3,4) and ^{20}Ne(n, $\alpha_0+\alpha_1$)^{17}O reactions, the values are the same.

CPC Accepted

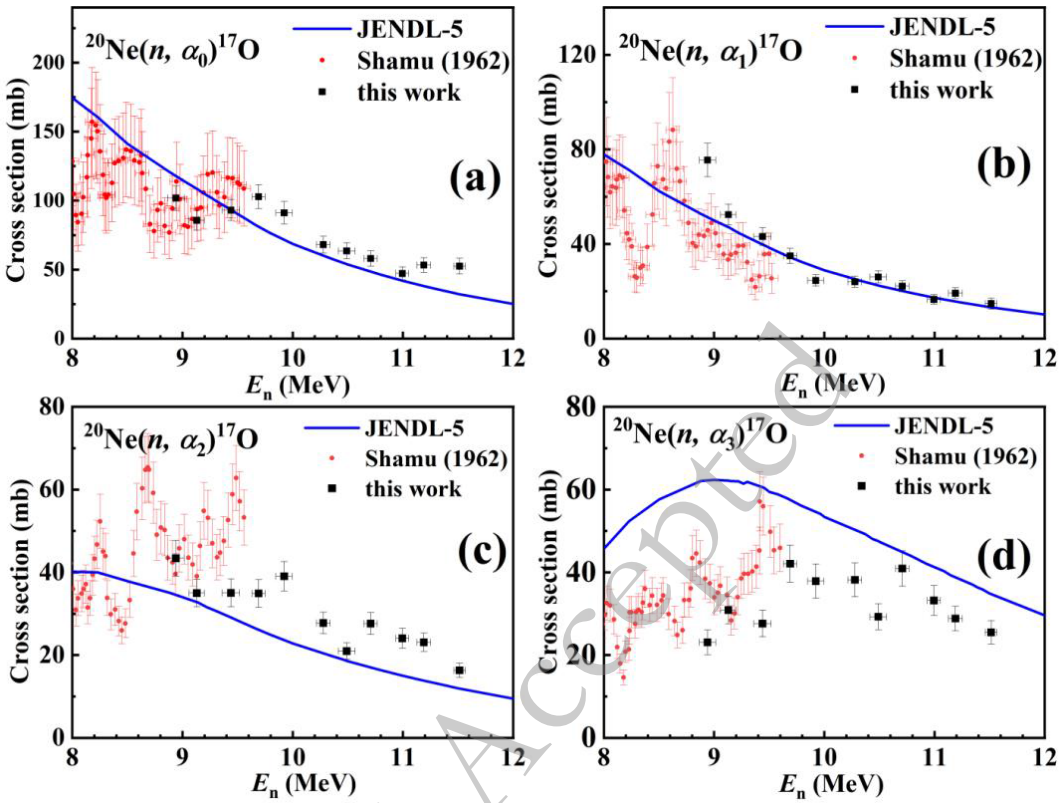


Fig. 7. (color online) Present cross sections of the ^{20}Ne(n, α_i)^{17}O (i=0,1,2,3) reactions compared with previous measurement data of Shamu *et al*. [11] and evaluation data in JENDL-5 [18].

CPC Accepted

are not completely smooth. In contrast, the α_3 channel shows an overall rise-and-fall behavior, with more pronounced fluctuations over the measured energy region. Compared with the data of Shamu *et al*. [11], the present results show smoother excitation functions with smaller uncertainties, about 8.2%~12.9% compared with approximately 15.0% in the previous work. The present measurement also extends the state-resolved α_0, α_1, α_2 and α_3 data from 9.6 MeV to 11.5 MeV. The present measurement also extends the state-resolved ^{20}Ne(n, α_i)^{17}O (i=0,1,2,3) cross section data from 9.6 MeV to 11.5 MeV. The smoother excitation functions mainly benefit from the improved event selection using the corrected anode-energy versus distance two-dimensional spectra, which enhances the separation of the α_i (i=0,1,2,3) event groups and reduces the influence of channel overlap. The smaller uncertainties are largely attributed to the more comprehensive correction procedure for detector efficiency, background interference, low-energy neutron interference, and non-uniformity of neutron-field distribution.

For the α_0 channel, the present data show a decreasing overall trend as the neutron energy increases, and are close to that of JENDL-5 [18]. However, around 8.94 – 9.44 MeV (three energy points), the present α_0 cross sections shows a local decrease followed by an increase. For the α_1 channel, the present cross sections decrease rapidly from 8.94 to 9.20 MeV, which differs from the JENDL-5 evaluation [18]. Above 9.2 MeV, the cross sections decrease more slowly and show good agreement with JENDL-5 [18]. For the α_2 channel, the present cross sections are systematically higher than the data in JENDL-5 [18]. While JENDL-5 [18] predicts a continuously decreasing excitation function, the present data shows oscillations around 9 – 12 MeV. The data of Shamu *et al*. [11] show large fluctuations in the α_2 channel and are generally higher than both the present data and the evaluation in the neutron energy region of 9.0 – 10.0 MeV. For the α_3 channel, the present cross sections are systematically lower than the data in JENDL-5 [18]. Similar with the α_2 channel, the present data shows oscillations around 9 – 12 MeV. Compared with the data of Shamu *et al.* [11], the present results provide a clearer constraint on both the magnitude and energy dependence of this channel.

Cross sections of the ^{20}Ne(n, α_0+α_1)^{17}O reaction were also obtained for the 11 energy points, as shown in Fig. 8, with better uncertainties than those of the ^{20}Ne(n, α_1)^{17}O reaction. In general, the present data are consistent with the sum of the cross sections of the ^{20}Ne(n, α_0)^{17}O and ^{20}Ne(n, α_1)^{17}O reactions in JENDL-5 [18]. This agreement indicates that the evaluated trend for the summed α_0+α_1 channel is reasonable in the present neutron-energy region. The present data are systematically higher than those of Shamu *et al*. [11], but they remain in agree-

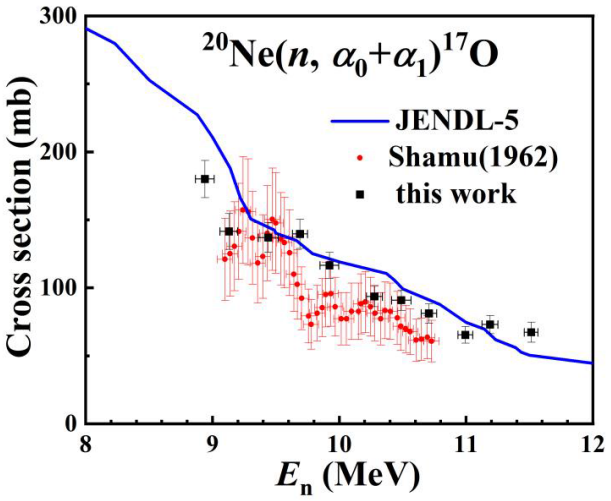


Fig. 8. (color online) Present cross sections of the ^{20}Ne(n, α_0+α_1)^{17}O reaction compared with the previous measurement data of Shamu *et al*. [11] and the evaluation data in JENDL-5 [18].

ment within the uncertainty ranges.

In general, the α_0 and α_1 results are reasonably consistent with those in JENDL-5 [18]. In contrast, the present α_2 cross sections are systematically higher than those in JENDL-5 [18], whereas the α_3 cross sections are generally lower. Since the α_2 and α_3 channels populate higher excited states in ^{17}O, their calculated cross sections may be more sensitive to the α-particle transmission coefficients, spin-parity coupling, and competition among open decay channels than those of the α_0 and α_1 channels. The generally good agreement observed for the α_0 and α_1 channels suggests that the overall magnitude of the ^{20}Ne(n, α)^{17}O reaction and the population of the lowest states in ^{17}O are reasonably described by the current evaluation. In contrast, the systematic differences observed for the α_2 and α_3 channels indicate that the predicted branching ratios among the excited states of ^{17}O may not be fully consistent with the experimental observations.

B. TALYS code analysis

Theoretical calculations for the ^{20}Ne(n, α_i)^{17}O (i=0,1,2,3) reaction were performed using the TALYS code [1]. TALYS provides a unified framework for the calculation of neutron-induced nuclear reaction cross sections by combining optical-model calculations, direct reaction contributions, pre-equilibrium emission, and Hauser-Feshbach compound-nucleus decay. In the present work, the TALYS calculations were performed primarily as a sensitivity study to investigate the influence of different model parameters on the state-resolved cross sections. Five TALYS-2.2 [30] model parameters were considered as shown in Table 3, and their values were used for generating 108 model sets (each set is a combination of all model parameters). A more detailed description of their meaning and available values may be found in Refs. [31,32].

The results of TALYS-2.2 [30] calculation are shown in Fig. 9. Shaded area represents the range covered by the 108 tested model combinations, the solid line represents the arithmetic mean of the calculations, and the black dashed line represents the selected best calculation. In addition, the red dashed line represents the evaluation data in JENDL-5 [18]. The best TALYS parameter set was selected according to a χ^2-based criterion. For each model combination, the average χ^2 value was calculated as

$$\chi^2 = \sum_{i=0}^{3}\sum_{j=1}^{N}\left(\frac{\sigma_{i,j}^{\rm cal}-\sigma_{i,j}^{\rm exp}}{\Delta\sigma_{i,j}^{\rm exp}}\right)^2, \quad (6)$$

where i denotes the (n, α_i) (i= 0,1,2,3) channel, j denotes the neutron-energy point, N is the number of measured neutron-energy points, $\sigma_{i,j}^{\rm cal}$ is the TALYS calculated cross sections, $\sigma_{i,j}^{\rm exp}$ is the measured cross sections, and $\Delta\sigma_{i,j}^{\rm exp}$ is the uncertainty of the measured cross sections. All measured data points for the four state-resolved channels were included in the comparison. No additional channel dependent weighting factor was applied. Therefore, the four channels were treated equally apart from the weighting by their individual experimental uncertainties. Among the tested model combinations, the parameter set with (*alphaomp* = 6, *ldmodel* = 1, *colenhance* = n, *widthmode* = 1, *preequilibrium* = y) gives the smallest overall deviation from the measured ^{20}Ne(n, α_i)^{17}O (i=0,1,2,3) cross sections.

Among the investigated parameters, the α-particle optical-model potential appears to have a significant influence on the calculated cross sections, because the α-particle transmission coefficients directly affect the probability of α emission from the compound nucleus. The level-density prescription also affects the calculated partial cross sections by modifying the statistical competition between the explicitly treated low-lying final states and the higher energy states of the compound nucleus ^{21}Ne. The better agreement obtained with (*ldmodel* = 1), corresponding to the Constant Temperature plus Fermi-gas level-density model in TALYS [30], indicates that this level-density prescription provides the most suitable description among the tested models for the statistical decay calculation in the present neutron-energy region. The inclusion of pre-equilibrium emission (*preequilibrium* = y) leads to improved agreement with the present measurement data. The preferred value (*colenhance* = n) further indicates that only introducing a global collective enhancement of the level density does not improve the description of the present state-resolved data within the tested TALYS framework.

The selected TALYS calculation reproduces the gen-

CPC Accepted

Table 3. List of TALYS model parameters and their values used for generating 108 model sets (Superscript "b" represents the selected best model parameters combination).

Parameter	Meaning	Values
alphaomp	Alpha optical model	5, 6^{b}, 8
ldmodel	Level density	1^{b}, 2, 5
colenhance	Collective enhancement	n^{b}, y
widthmode	Width fluctuation corrections	0, 1^{b}, 2
preequilibrium	Pre-equilibrium reaction mechanism	n, y^{b}

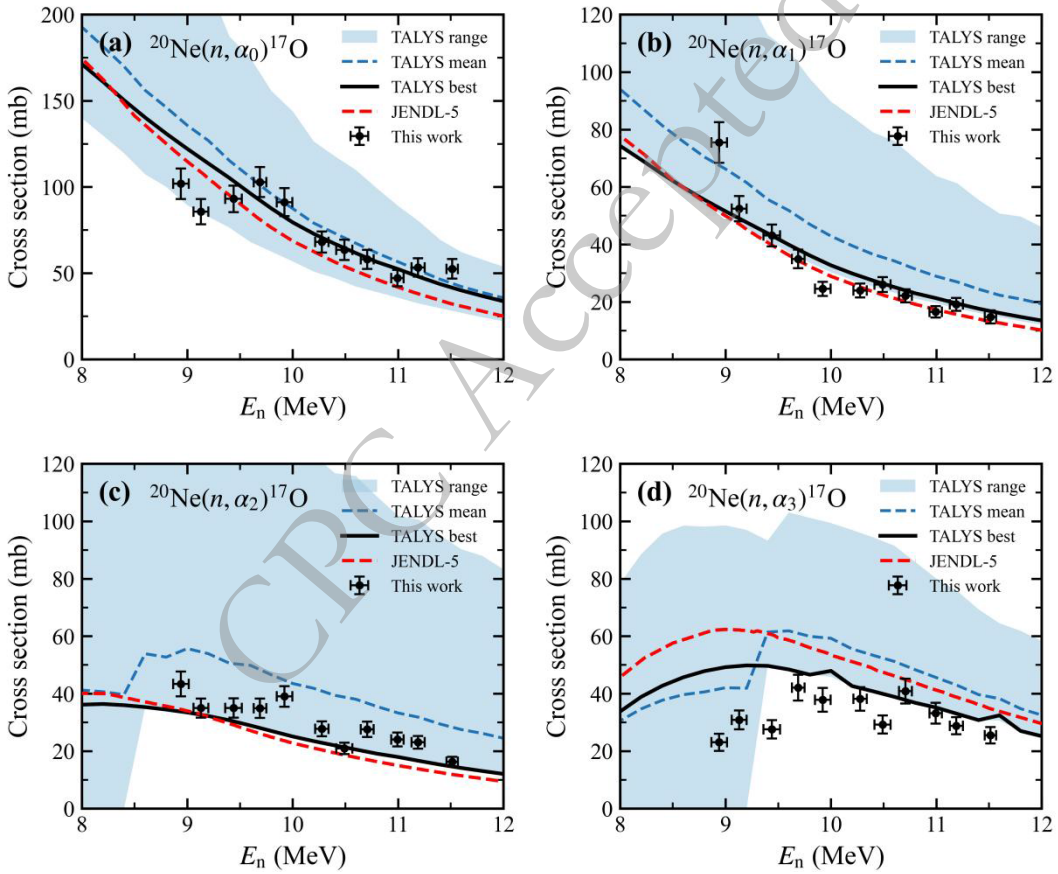


Fig. 9. (color online) TALYS-calculated cross sections for the ^{20}Ne(n, α_i)^{17}O (i=0,1,2,3) reactions compared with the measured data and the evaluated data from JENDL-5 [18].

eral decreasing trend of the measured α_0 and α_1 cross sections in the 8–12 MeV region. The α_2 channel shows a larger model dependence, but most of the experimental data are covered by the calculated model band. For the α_3 channel, the TALYS calculated results are higher than the measured results in the 8–12 MeV region. Additional checks were performed to examine possible experimental contributions to the discrepancy between the results of measured data and TALYS calculations. To estimate the influence of the PHD-related event-selection boundary, the anode-energy selection range of the selected event regions was varied by 0.02 MeV. This value corresponds to the largest reasonable boundary variation that can be applied while maintaining a reliable separation of neighboring event groups. A larger variation would lead to severe overlap between adjacent event regions and would no longer represent a reasonable event-selection uncertainty. The resulting variation of the extracted α_3 cross sections is 2.4%–3.6%, which was included in the uncertainty of N_α. Possible contributions from the α_4 and α_5 events to the selected α_3 region were also considered and it found to be smaller than 7%. The low-energy neutron correction for α_3 mainly arises from low-energy neutron induced α_0 events entering the selected α_3 region. This contribution exceeds 10% only for the four neutron energy points, namely 8.93, 9.13, 9.43, and 9.68 MeV, and is not

CPC Accepted

significant above 10 MeV. Therefore, the experimental effects considered here are unlikely to fully account for the systematic overestimation of the α_3 cross section by the TALYS calculations. For TALYS calculation, the overestimation of the α_3 cross section is likely related to two factors. First, α_3 populates a higher excited state of ^{17}O, resulting in a lower outgoing α-particle energy and stronger sensitivity to the Coulomb-barrier penetrability and the α optical potential. Second, the population of this state depends on spin-parity coupling and the detailed structure of the ^{21}Ne*, which may not be fully described by a global Hauser-Feshbach calculation. Although the present TALYS analysis does not uniquely determine the underlying reaction mechanism, it demonstrates the usefulness of the present experimental data for constraining model calculations and for evaluation of nuclear data. Further theoretical investigations would be valuable for clarifying the roles of the α-particle optical-model potential, level-density prescription, pre-equilibrium processes and global collective enhancement in the ^{20}Ne(n, α)^{17}O reaction.

V. CONCLUSIONS

Cross sections for the ^{20}Ne(n, α_i)^{17}O (i=0,1,2,3) reactions were measured in the neutron-energy region of 8.9 – 11.5 MeV (11 energy points) using a twin GIC. The GIC was filled with a neon-based gas mixture, in which the natural neon component served as the reaction sample, while the chamber was used for charged particle detection. The present measurement provides new α_0, α_1, α_2 and α_3 partial cross-section data from 9.6 to 11.5 MeV, where previous measurement results are limited to the summed α_0+α_1 cross sections. The summed ^{20}Ne(n, α_0+α_1)^{17}O cross sections were also determined from the combined α_0+α_1 yields, providing a more reliable cross-section quantity for comparison with previous measurements and evaluation data. Compared with previous measurements, the present work provides several improvements in the data analysis. First, the corrected anode-energy versus distance two-dimensional spectra were used for event selection, which improved the separation of the α_0, α_1, α_2 and α_3 event groups. Second, detailed Monte Carlo simulations were performed to determine the anode detection efficiency, detection efficiency for distance, background interference correction, low-energy neutron interference correction, non-uniformity of neutron-field distribution and the effective number of ^{20}Ne nuclei. These improvements reduce the uncertainties associated with detector efficiency and background subtraction and enable a more reliable extraction of the state-resolved ^{20}Ne(n, α_i)^{17}O (i=0,1,2,3) cross sections. The measured α_0+α_1 cross sections show a clear decreasing trend with increasing neutron energy and are generally consistent with the evaluation data in JENDL-5 [18]. Both individual α_0 and α_1 cross sections decrease as the neutron energy increases and are reasonably consistent with the data in JENDL-5 [18]. In contrast, for α_2 and α_3 cross sections, significant deviations between the present data and those in JENDL-5 library [18] are observed: The present α_2 cross sections are systematically higher than those in JENDL-5 in most of the measured energy region, whereas the α_3 cross sections are generally lower than those in JENDL-5 [18]. In detail, the JENDL-5 evaluation [18] does not fully capture the pronounced fluctuations observed in the measured excitation functions. Analysis using TALYS-2.2 [30] shows that the measured α_0, α_1, α_2 and α_3 cross sections provide sensitive constraints on the parameters of α-particle optical potential, level-density, width-fluctuation, and pre-equilibrium contribution. The TALYS-2.2 calculations can describe the measured α_0, α_1 and α_2 cross sections, whereas the calculated α_3 cross sections overestimate the measured data in the 8–12 MeV region. The present cross sections for the ^{20}Ne(n, α_i)^{17}O (i=0,1,2,3) reactions and the ^{20}Ne(n, α_0+α_1)^{17}O reaction can provide detailed information on the population of individual states in ^{17}O. The observed discrepancies with the JENDL-5 evaluation [18] for the α_2 and α_3 channels demonstrate that state-resolved experimental data are essential for testing and improving nuclear reaction models. The dataset reported in the present work therefore constitutes an important benchmark for future evaluations of neutron-induced reactions on ^{20}Ne and for further developments of Hauser–Feshbach-based reaction calculations.

APPENDIX A: THE MEASURED CROSS SECTIONS FOR THE ^{20}Ne(n, α)^{17}O REACTION

Table A1. The measured cross sections for the ^{20}Ne(n, α)^{17}O reaction.

E_n (MeV)	Cross Sections (mb)				
	^{20}Ne(n, α_0)^{17}O	^{20}Ne(n, α_1)^{17}O	^{20}Ne(n, α_2)^{17}O	^{20}Ne(n, α_3)^{17}O	^{20}Ne(n, α_0+α_1)^{17}O[a]
8.94±0.07	101.87±8.84	75.48±7.07	43.41±4.32	23.10±2.98	180.00±13.66
9.13±0.07	85.70±7.33	52.42±4.39	34.99±3.31	30.88±3.31	141.43±13.15

Continued on next page

CPC Accepted

Table A1-continued from previous page

E_n (MeV)	Cross Sections (mb)				
	^{20}Ne(n, α_0)^{17}O	^{20}Ne(n, α_1)^{17}O	^{20}Ne(n, α_2)^{17}O	^{20}Ne(n, α_3)^{17}O	^{20}Ne(n, α_0+α_1)^{17}O[a]
9.44±0.08	93.10±7.65	43.13±3.78	35.04±3.38	27.62±3.22	136.97±10.95
9.69±0.06	102.86±8.75	34.95±3.24	34.90±3.36	42.08±4.48	139.57±10.70
9.92±0.07	91.18±8.14	24.56±2.44	39.04±3.57	37.88±4.12	116.50±9.55
10.28±0.06	68.09±6.11	24.01±2.41	27.77±2.59	38.19±4.09	93.67±7.47
10.49±0.08	63.59±5.88	26.05±2.59	20.97±1.97	29.27±3.14	90.94±7.47
10.71±0.06	58.08±5.53	22.13±2.31	27.61±2.64	40.92±4.30	81.19±7.07
10.99±0.06	47.19±4.73	16.56±2.02	24.06±2.42	33.20±3.59	65.39±6.09
11.19±0.06	53.33±5.34	19.18±2.25	23.09±2.21	28.84±2.98	72.99±6.75
11.51±0.05	52.52±5.68	14.79±2.31	16.31±1.72	25.51±2.84	67.37±7.40

[a] The ^{20}Ne(n, α_0+α_1)^{17}O cross sections were obtained from the combined ^{20}Ne(n, α_0+α_1)^{17}O event yields in the uncorrected anode-energy spectrum, not from the arithmetic sum of the separate ^{20}Ne(n, α_0)^{17}O and ^{20}Ne(n, α_1)^{17}O cross sections.

CPC Accepted

References

[1] A. Koning, S. Hilaire, and S. Goriely, Eur. Phys. J. A **59**, 131 (2023),
[2] F. Hammache, P. Adsley, L. Lamia, *et al.*, Phys. Rev. Lett. **132**, 182701 (2024),
[3] A. Best, M. Beard, J. Görres, *et al.*, Phys. Rev. C **87**, 045805 (2013),
[4] J. Frost-Schenk, P. Adsley, A. M. Laird, *et al.*, Monthly Notices of the Royal Astronomical Society **514**, 2650 (2022),
[5] W. Y. Xin, C. M. Yip, K. Nomoto, *et al.*, Nucl. Sci. Tech. **37**, 146 (2026),
[6] B. Zhou, Y. Funaki, H. Horiuchi, *et al.*, Nat. Commun **14**, 8206 (2023),
[7] A. K. Nurmukhanbetova, V. Z. Goldberg, D. K. Nauruzbayev, *et al.*, Phys. Rev. C **100**, 062802 (2019),
[8] XUNDL, https://www.nndc.bnl.gov/ensdf/xundl/index.jsp.
[9] C. H. Johnson, C. K. Bockelman, and H. H. Barschall, Phys. Rev. **82**, 117 (1951),
[10] R. J. Bell, T. W. Bonner, and F. Gabbard, Nuclear Physics **14**, 270 (1959),
[11] R. E. Shamu, Nuclear Physics **31**, 166 (1962),
[12] M. Cevolani, S. Petralia, and G. Di Caporiacco, Nuc. Phys. **79**, 379 (1966),
[13] W. N. McDicken and W. Jack, Nuc. Phys. **88**, 457 (1966),
[14] S. Kardonsky, H. L. Finston, and E. T. Williams, Phys. Rev. C **4**, 846 (1971),
[15] *EXFOR Data (S. Y. Lin), https://www-nds.iaea.org/exfor/servlet/X4sGetSubent?reqx=30213&subID=30240002.*
[16] V. A. Khryachkov, I. P. Bondarenko, B. D. Kuzminov, *et al.*, Phys. Atom. Nuclei **75**, 404 (2012),
[17] ENDF, https://www-nds.iaea.org/exfor/endf.html.
[18] O. Iwamoto, N. Iwamoto, S. Kunieda, *et al.*, Journal of Nuclear Science and Technology **60**, 1 (2023),
[19] Y. Hu, Yu. M. Gledenov, Z. Cui, *et al.*, Eur. Phys. J. A **60**, 51 (2024),
[20] C. Xia, Z. Chen, Y. Hu, *et al.*, Eur. Phys. J. A **61**, 246 (2025),
[21] S. Agostinelli, J. Allison, K. Amako, *et al.*, Nucl. Instrum. Meth. Phys. Res. A **506**, 250 (2003),
[22] H. Jiang, Z. Cui, Y. Hu, *et al.*, Chin. Phys. C **44**, 114102 (2020),
[23] H. Bai, H. Jiang, Y. Lu, *et al.*, Applied Radiation and Isotopes **152**, 180 (2019),
[24] H. Bai, Z. Wang, L. Zhang, *et al.*, Nucl. Instrum. Meth. Phys. Res. A **886**, 109 (2018),
[25] H. Bai, Z. Wang, L. Zhang, *et al.*, Nucl. Instrum. Meth. Phys. Res. A **863**, 47 (2017),
[26] C. Xia, Y. Hu, J. Liu, *et al.*, Eur. Phys. J. A **62**, 3 (2026),
[27] M. Peck, A. Göök, J. Enders, *et al.*, Nucl. Instrum. Meth. Phys. Res. A **919**, 105 (2019),
[28] *ENDF/B-VIII. 1, https: //www. osti. gov/biblio/2571019. https://doi.org/10.11578/endf/2571019.*
[29] A. D. Carlson, V. G. Pronyaev, R. Capote, *et al.*, Nucl. Data Sheets **148**, 143 (2018),
[30] TALYS-2.2, https://nds.iaea.org/talys/.
[31] D. Rochman, A. Koning, S. Goriely, *et al.*, Nuclear Physics A **1053**, 122951 (2025),
[32] P. Žugec, N. Colonna, D. Rochman, *et al.*, Phys. Let. B **868**, 139713 (2025),